Constructing an idealized model of the North Atlantic Ocean using slippery sacks

Patrick T. Haertel [a,*], Luke Van Roekel [b], Tommy G. Jensen [c,1]

[a] Department of Geology and Geophysics, Yale University, P.O. Box 208109, New Haven, CT 06511, USA
[b] Department of Atmospheric Science, Colorado State University, USA
[c] International Pacific Research Center, University of Hawaii at Manoa, USA

ARTICLE INFO

ABSTRACT

This paper documents the continued development and testing of a new Lagrangian oceanic general circulation model. The slippery sacks ocean model (SSOM), which represents a body of water as a pile of conforming parcels, is improved and is used to simulate circulations in homogeneous oceans and in an idealized model of the North Atlantic Ocean.

A method for including horizontal mixing in the SSOM is presented. A given sack's nearest neighbors are identified in the positive and negative x- and y-directions, and the sack exchanges momentum and/or tracers with these neighbors. This formulation of mixing is straightforward to implement, computationally efficient, and it produces results similar to a standard Eulerian finite-difference representation of diffusion.

The model's ability to reproduce the Stommel and Munk solutions to the classical western boundary current problem is tested. When steps are taken to reduce the potential energy barrier to sacks crossing one another, the model generates circulations that are consistent with linear theory. In moderately non-linear regimes the model produces appropriate departures from linear solutions including a boundary current that continues along the northern boundary for a time.

Taking advantage of the new mixing scheme and lessons learned from simulations of homogeneous oceans, the authors construct an idealized model of the North Atlantic Ocean. They compare simulations conducted with the SSOM to similar simulations conducted with the Massachusetts Institute of Technology general circulation model (MITgcm). The SSOM and the MITgcm produce similar wind-forced gyres, thermocline structure, and meridional overturning. The SSOM is also used to explore how circulations change in the limit when tracer diffusion goes to zero.

© 2008 Elsevier Ltd. All rights reserved.

1. Introduction

This paper is the third in a series that describes the development of a new ocean model that represents a body of water as a pile of conforming parcels, or "slippery sacks." The numerical method that is the basis for the model is outlined by Haertel and Randall (2002; hereafter HR02). The first application of the model to a "real world" problem, upwelling in a large lake, is described by Haertel et al. (2004; hereafter H04). In this study we further develop the slippery sacks ocean model (SSOM), and use it to simulate large scale ocean circulations for the first time. After testing the SSOM's ability to reproduce flows in classical models of western boundary currents, we simulate circulations in an idealized model of the North Atlantic Ocean. In this section we provide motivation

for this study, and we review classical theory of western boundary currents.

1.1. Motivation

There are a number of advantages to using a fully Lagrangian ocean model. First, and most obvious, is that such a model can maintain the adiabatic property of advection (Griffies et al., 2000) and exactly conserve every moment of tracer distributions. Another related advantage is that the advection of an arbitrary number of tracers requires a fixed number of calculations. When a parcel's position is updated, all tracers are moved along with the parcel. A third advantage is that trajectory information is provided for all water parcels in the ocean without any extra computations. For these reasons it is likely that a fully Lagrangian ocean model would be quite useful for studies that require careful treatment of tracer mixing (e.g., Ito and Deutsch, 2006), a great number of tracers, or detailed analysis of parcel trajectories. Experiments conducted with the SSOM have revealed several other more subtle advantages that do not necessarily apply to all Lagrangian models:

---

(1) including arbitrarily complicated bottom topography with irregular coastlines and islands adds no complexity to simulations; (2) horizontal boundaries of bodies of water occur where the free surface meets the coastline, and these can move as they do in nature; (3) it is easy to implement Eulerian vertical mixing schemes in the Lagrangian framework.

The above advantages provide motivation for the continued development of the SSOM. However, the road to a full-fledged fully-Lagrangian oceanic general circulation model is a long one, with a number of remaining obstacles. The general nature of the challenge we face is best described with the following metaphor: the slippery sacks model is the platypus of ocean models. Many features of the model are so radically different from conventional ocean models that developing each component of the SSOM requires creative engineering. While we have come up with adequate solutions for the treatment of the pressure force (HR02) and vertical mixing (H04), remaining challenges include implementing horizontal mixing in a simple and computationally efficient manner, validating the model for a broad range of oceanic flows, and identifying and addressing new numerical issues that are unique to the slippery sacks framework.

In this study we use the SSOM to simulate circulations in homogeneous oceans and in an idealized model of the North Atlantic Ocean. Even though many of the simulations we present are quite idealized (e.g., of essentially two-dimensional circulations in homogeneous oceans), this work has yielded progress in each of the remaining challenges listed above: (1) prior to this study the SSOM had not been used to simulate western boundary currents; (2) a form of horizontal diffusion is implemented for this study; (3) a new numerical issue is identified and addressed with the simulations presented here; and (4) this is the first study that examines the SSOM's ability to simulate meridional overturning. Therefore this study represents a few more important steps down the road toward the development of a full-fledged Lagrangian ocean model, which promises to have some unique capabilities that distinguish it from all other models.

1.2. Classical theory of western boundary currents

In this section we review classical analytic solutions to the western boundary current problem, which we compare to SSOM simulations later in this paper. However, it should be emphasized that the SSOM does not solve the vorticity equation discussed below, but rather the more general Lagrangian equations discussed in Section 2. Moreover, the homogeneous ocean simulated with the SSOM has sloping basin walls, whereas the box ocean described below has vertical walls. Despite these differences, we would expect the SSOM to be able to produce circulations similar to those specified by the analytic solutions presented below.

Consider a box-shaped ocean of constant depth D and width and length L on a β-plane. For simplicity we assume that the ocean has constant density ρ and that the surface stress acts as a body force on a column of water. We also assume that there are two types of friction: linear damping of velocity (i.e., bottom friction) and horizontal viscosity. Then the following equation approximates the evolution of the vertical component of vorticity (e.g., Pedlosky, 1996, Eq. (2.2.9)):

$$\frac{\partial}{\partial t}\nabla^2\psi + J(\psi, \nabla^2\psi) + \frac{\partial\psi}{\partial x} = (\nabla\times\tau)_z - k\nabla^2\psi + v\nabla^4\psi \qquad (1)$$

where $\psi = \psi(x, y, t)$ is the stream function ($u = -\partial\psi/\partial y$ and $v = \partial\psi/\partial x$ were u, v are velocity components), J denotes the Jacobian operator, τ is the surface wind stress, k is the linear damping coefficient, and v is the horizontal viscosity coefficient. The vari-

ables in (1) have been non-dimensionalized by selecting L, $(\beta L)^{-1}$, βL^3, βL, βL^3, and $\beta^2 L^3\rho D$ as units for horizontal distance, time, the stream function, linear damping, viscosity, and the surface stress, respectively. Note that (1) neglects the divergence of vorticity, which is equivalent to assuming there is a rigid lid on top of the ocean. The western and southern boundaries of the ocean are placed along $x = 0$ and $y = 0$, respectively, which means that the eastern and northern boundaries are at $x = 1$ and $y = 1$, respectively. We consider an idealized forcing consistent with easterly winds over the southern half of the basin and westerly winds over the northern half:

$$\tau = (-\tau_0\cos(\pi y), 0) \qquad (2)$$

Variations of this seemingly simple dynamical system have been the subject of numerous studies (e.g., Pedlosky, 1996, Chapter 2). In most cases solutions include intense western boundary currents that are reminiscent of ocean currents such as the Gulf Stream and the Kuroshio. While (1) and (2) obviously lack many features of real oceans (e.g., variable bathymetry, density variations), they appear to capture the most fundamental dynamics responsible for western boundary currents. Moreover, the simplicity of this system and the degree to which it has been studied make it an excellent test case for a new ocean model.

Analytic solutions to (1) and (2) can be obtained by neglecting non-linear terms, setting $\psi = 0$ on the boundary (i.e., assuming that the boundary is a streamline), and solving for a steady state. Below we review two linear solutions for special cases that we simulate with the slippery sacks model later in this paper.

(1) Stommel solution

Stommel (1948) provided the first solution to the western boundary current problem. His solution to (1) and (2), which neglects viscosity, is as follows (adapted from Krauss (1973, p. 265)):

$$\psi = \frac{\tau_0}{k\pi}\sin(\pi y)\left[1 - \frac{e^{(1-x)/2k}\sinh(\alpha x) + e^{-x/2k}\sinh(\alpha(1-x))}{\sinh(\alpha)}\right] \qquad (3)$$

where $\alpha = \sqrt{1/(4k^2) + \pi^2}$. Fig. 1a shows the stream function for $k = 0.05$. There is a broad region of relatively weak southward flow in the eastern portion of the basin. Here the advection of basic state vorticity (the last term on the left hand side of (1)) is approximately balanced by the generation of vorticity by the wind stress (the first term on the right hand side of (1)) as found by Sverdrup (1947). Along the western boundary there is a relatively intense northward current, with a non-dimensional width approximately equal to k. Stommel (1948) noted the general similarity of this flow pattern with what occurs in oceans, and that it differs from the solution given a constant Coriolis force, which is a symmetric gyre.

(2) Munk solution

Munk (1950) formulated the western boundary current problem in a different way. He replaced linear friction with harmonic viscosity (i.e., which corresponds to setting $k = 0$ in (1) and (2) and using $v > 0$), and changed the boundary condition from free-slip to no-slip. The Munk problem can also be formulated with a free-slip boundary condition, which is what we use here, and in that case the first-order asymptotic solution to (1) and (2) is as follows (Pedlosky, 1987, Chapter 5):

$$\psi = \tau_0\pi(1-x)\sin(\pi y)\left[1 - e^{-x/(2\delta_m)}\left(\cos\frac{\sqrt{3}x}{2\delta_m} + \frac{1}{\sqrt{3}}\sin\frac{\sqrt{3}x}{2\delta_m}\right)\right] \qquad (4)$$

where $\delta_m = v^{1/3}$ is the Munk boundary layer scale. Fig. 1b shows the solution for $\delta_m = 0.05$. As seen in the Stommel solu-
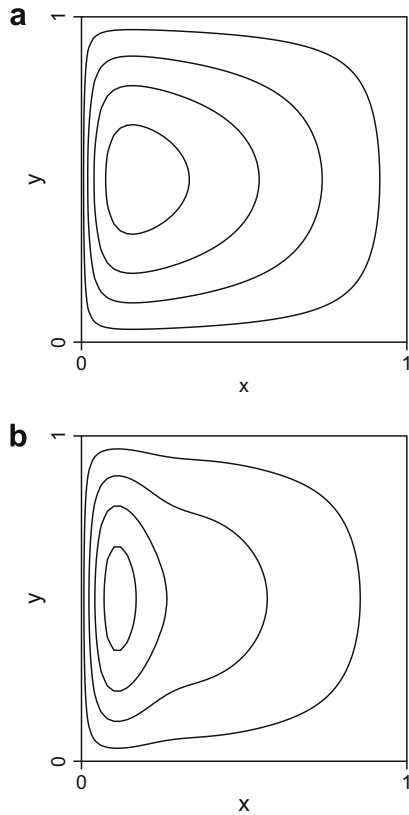
Fig. 1. Analytic solutions to the western boundary current problem for $\tau_0 = 10^{-5}$. (a) Stream function for the Stommel solution ($k = 0.05$, $v = 0$, contours: $\psi = 2.5, 7.5, 12.5, 17.5 \times 10^{-6}$). (b) Stream function for the Munk solution ($k = 0$, $\delta_m = 0.05$, contours: $\psi = 4.5, 13.5, 22.5, 31.5 \times 10^{-6}$).

tion there is southward flow in most of the basin, and an intense northward current along the western boundary. However, unlike the Stommel solution, there is a strong offshore counter current as well.

1.3. Outline of this paper

In this study we test the slippery sacks model's ability to spin up circulations similar those shown in Fig. 1 in homogeneous oceans, and then we model similar gyres as well as deep overturning in an idealized model of the North Atlantic Ocean. Section 2 describes how we configure the model for simulations of homogeneous oceans. Section 3 describes a new horizontal mixing scheme. Section 4 discusses the existence of a potential energy barrier to circulations in piles of slippery sacks, and how this barrier and can be overcome. In Section 5 simulations of the Stommel and Munk solutions for homogeneous oceans are compared with analytic solutions. Simulations of circulations in an idealized model of the North Atlantic Ocean are presented in Section 6. Section 7 is a summary and discussion.

2. Model configuration for homogeneous oceans

Many of the simulations presented in this paper are of homogeneous oceans driven by idealized wind forcings. The assumption of constant density simplifies the equations of motion for slippery sacks. In this section we present these equations in simplified form, and we describe several other aspects of our model configuration specific to homogeneous ocean simulations.

2.1. Equations of motion

For a detailed description of equations of motion for slippery sacks the reader is referred to HR02 and H04. Here we outline a simplified version appropriate for homogeneous oceans. Horizontal positions $\mathbf{x}_i$ and velocities $\mathbf{v}_i$ of sacks are predicted using classical mechanics:

$$\frac{d\mathbf{x}_i}{dt} = \mathbf{v}_i \tag{5}$$

$$\frac{dv_i}{dt} + f\mathbf{k} \times \mathbf{v}_i = \frac{\mathbf{F}_{p_i}}{M_i} + \mathbf{a}_{f_i} + \frac{\tau}{\rho D} \tag{6}$$

where i is the sack index, t is time, f is the Coriolis parameter, $\mathbf{k}$ is the unit vector in the vertical, $\mathbf{F}_{p_i}$ the horizontal force on sack i resulting from pressure, $\mathbf{a}_{f_i}$ is the acceleration due to friction, M_i is the mass of sack i, ρ is density, and τ is the surface wind stress. The last term in (6) essentially applies the surface wind stress as a body force on a column of water; each sack feels a portion of the surface wind stress proportional to the cross-sectional area it would have if it were a column of water extending from the surface to the bottom.

Each slippery sack is assumed to have a horizontal mass distribution m_i that is constant with respect to time in the sack's frame of reference. We use the mass distribution function provided by H04:

$$m_i(x,y) = \frac{M_i}{r_x r_y} s\left(\frac{|x|}{r_x}\right) s\left(\frac{|y|}{r_y}\right) \tag{7}$$

where r_x and r_y are the sack radii in the x- and y-directions, respectively, and the sack shape function $s(d) = 1 + (2d - 3)d^2$ for $d < 1$ and $s(d) = 0$ for $d \geqslant 1$. This distribution is roughly shaped like a bell, but it is not axisymmetric. A sack's vertical thickness H_i can be formulated in terms of the mass distribution as follows:

$$H_i(\mathbf{x}) = \frac{m_i(\mathbf{x} - \mathbf{x}_i)}{\rho} \tag{8}$$

and the horizontal force on a sack resulting from hydrostatic pressure is

$$\mathbf{F}_{p_i} = \int \rho g \nabla H_i \left(b + \sum_{j=1}^{n} H_j \right) dA \tag{9}$$

where the integral is evaluated over the horizontal projection of sack i, g is gravity, n is the total number of sacks, b is the height of the bottom topography, and A is the horizontal area measure. The frictional acceleration results from linear damping of velocity and horizontal viscosity:

$$\mathbf{a}_{f_i} = -kv_i + \mathbf{a}_{v_i} \tag{10}$$

where the calculation of $\mathbf{a}_{v_i}$ is discussed below.

2.2. Non-dimensional coordinates

In order to make the western boundary current simulations as general as possible, and, in particular, to make it easy to compare them with the analytic solutions discussed in Section 1, we use the non-dimensional coordinate system defined for (1), which means selecting L, $(\beta L)^{-1}$, and $\beta^2 L^3 \rho D$ as units for horizontal distance, time, the surface stress, respectively. We also select D, $DL^2\rho$ and $L^4\beta^2/D$ as units of vertical distance, mass and gravity, respectively, and set $f = \beta y$. Then (5)–(9) become:

$$\frac{d\tilde{\mathbf{x}}_i}{d\tilde{t}} = \tilde{v}_i \tag{11}$$

$$\frac{d\tilde{v}_i}{d\tilde{t}} + \tilde{y}\mathbf{k} \times \tilde{v}_i = \frac{\tilde{\mathbf{F}}_{p_i}}{\tilde{M}_i} + \tilde{\mathbf{a}}_{f_i} + \tilde{\tau} \tag{12}$$

$$\tilde{m}_i(\tilde{x}, \tilde{y}) = \frac{\tilde{M}_i}{\tilde{r}_x \tilde{r}_y} s\left(\frac{|\tilde{x}|}{\tilde{r}_x}\right) s\left(\frac{|\tilde{y}|}{\tilde{r}_y}\right) \tag{13}$$
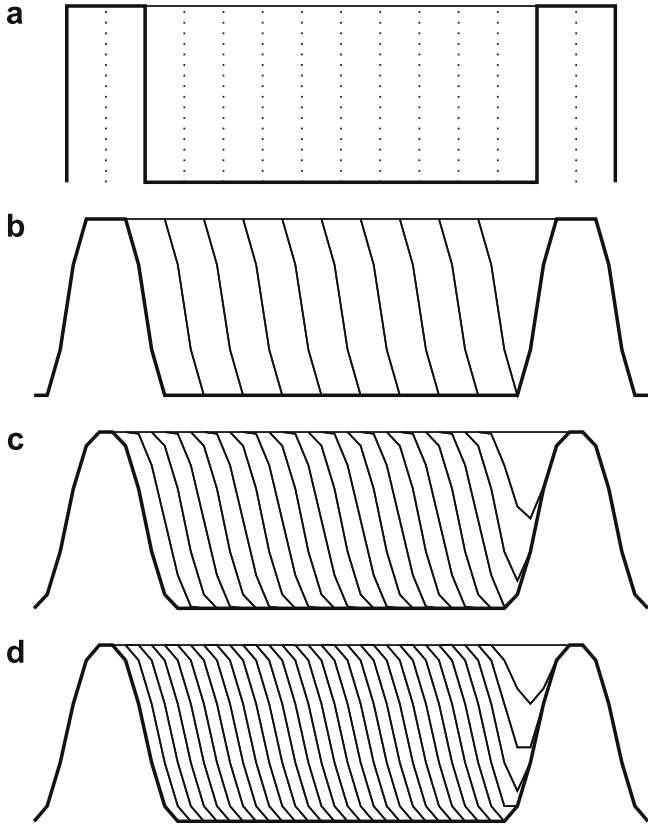
Fig. 2. An illustration of the initialization technique. In all panels the heavy line denotes the bottom surface and light solid lines are sack outlines. (a) a rectangular body of water bordered by rectangular walls, both of which are sliced along the dotted lines. (b)–(d) Sack outlines and bathymetry for initial states with overlap parameters of 1, 2, 3, respectively. For each case the sack radius is 1/10 of the initial basin width.

$$\tilde{H}_i(\tilde{\mathbf{x}}) = \tilde{m}_i(\tilde{\mathbf{x}} - \tilde{\mathbf{x}}_i) \tag{14}$$

$$\tilde{\mathbf{F}}_{p_i} = \int \tilde{g}\nabla\tilde{H}_i\left(\tilde{b} + \sum_{j=1}^{n}\tilde{H}_j\right)\tilde{d}A \tag{15}$$

where the tilde ($\sim$) notation denotes non-dimensional variables.

The non-dimensional slippery sacks simulations presented below are not intended to apply to an entire ocean; rather, the parameters we choose are based on the assumption that the collection of sacks is representing the upper layer of an ocean.[2] For most of the simulations we assume $D = 200$ m, $L = 5000$ km, $\rho = 1000$ kg m^{-3}, $\beta = 2.28 \times 10^{-11}$ m^{-1} s^{-1}, $\tau_0 = 10^{-5}$, and $\tilde{g} = 0.0005 - 0.001$. These values equate to an actual wind stress amplitude of 0.13 N m^{-2}, and values of gravity 6–12 times less than that on earth. Using a low value of gravity in a homogeneous ocean is analogous to employing gravity retardation in a more realistic setting (GWR; Jensen, 1996, 2001, 2003; H04). This technique has been used in ocean and lake simulations to increase computational efficiency by allowing longer time steps, but it does have side effects, such as greatly amplifying free surface height perturbations.[3] In Section 6 we discuss the consequences of using GWR in our idealized model of the North Atlantic Ocean.

Eqs. (11)–(15) are solved using split time-differencing (H04); the forward scheme is used for the viscous acceleration, and

third-order Adams-Bashforth time-differencing is used for the other terms. The integral in (15) is approximated with a Riemann sum which leads to the conservation of energy in the limit as the time step approaches zero and requires $O(n)$ operations to evaluate for n sacks (HR02; H04).

2.3. Initialization

Representing a box-shaped body of water is a challenge for the slippery sacks model; it is better suited to bodies of water with more realistic sloping bathymetry. We use the initialization method developed by HR02 for the spreading ridge problem (see their Fig. 3). To illustrate the technique we apply it to a rectangular two-dimensional body of water bounded by walls on each side (Fig. 2a). We divide the water and the walls into columns of equal width, and then convert each column into a slippery sack with the mass distribution referenced above. The initial bathymetry is constructed by stacking the wall sacks, and when the water sacks are placed into the basin the free surface is perfectly level (Fig. 2b). The resulting basin and pile of slippery sacks amount to horizontally smoothed versions of the rectangular ocean and rectangular topography (Fig. 2a and b). For the initialization depicted in Fig. 2b the sack radius is selected to be equal to a column width, so that each sack overlaps only one neighbor on each side. Alternatively, the sack radius can be selected to be two or three times as wide as a column (but it must be an integral multiple of the column width in order to obtain a perfectly level free surface) yielding a pile of sacks with a greater degree of overlap (Fig. 2c and d). Hereafter, we refer to the sack overlap parameter as the ratio of the sack radius to the column width (i.e., Fig. 2b–d correspond to overlap parameters of 1, 2, 3, respectively). It turns out that properly adjusting this parameter is important for facilitating circulations in piles of sacks. We have described the initialization technique for a two-dimensional body of water for simplicity – it works the same way for three dimensions (3D) except that the water and walls are sliced in both the x- and y-directions and the resulting box-shaped columns are converted into 3D sacks.

3. Horizontal mixing

One of the important new features of the SSOM developed for this study is a scheme for horizontal mixing, which is patterned after the implementation of vertical mixing discussed by H04. Sacks are first partitioned into layers, and then individual layers are divided into rows parallel to each horizontal axis, and sacks are allowed to exchange momentum and/or tracers with their nearest neighbors in a given row.[4] We first describe how the mixing scheme works for a single layer of sacks, and then discuss how it is applied in three-dimensional simulations.

3.1. Mixing in a single layer

Horizontal fluxes in a given layer of sacks are calculated separately for the x- and y-directions. To illustrate the method we discuss the x-flux in detail. At the beginning of a time step the horizontal domain of the model is divided into rectangular sections that run parallel to the x-axis and span the entire x-domain. Sacks whose centroids lie in a given section are allowed to mix properties with their nearest neighbor on each side, where "nearest" means

---

[2] If D were defined to be the actual depth of an ocean, velocities would be too weak, and non-linear effects would be underestimated (Bryan, 1963).

[3] Perturbations to surface elevations become large because GWR essentially reduces the density difference between the water and the air above it.

[4] We actually only use this scheme to mix momentum (and not tracers) for the simulations presented in later sections. However, we illustrate the scheme by applying it to a hypothetical tracer for simplicity. Preliminary experiments suggest that the scheme works in realistic applications for tracers as well; however, we have not thoroughly tested for potential side effects such as the clustering of sack densities around a discrete set of values.

the sack having the smallest deviation in x-position. For example, consider an intensive fluid property q and let Q denote the flux of q in the x-direction. The following formula is used to calculate the flux between adjacent sacks i and $i+1$:

$$Q_{i+1/2} = v \frac{q_{i+1} - q_i}{|\mathbf{x}_{i+1} - \mathbf{x}_i|} \rho dA \tag{16}$$

where v is the coefficient of mixing, dA is the cross-sectional area of the portion of the layer of sacks lying over the rectangular section, and the vertical bars denote the distance metric. Note that if the sacks have the same y-position, this flux is identical to the standard second-order finite-difference diffusive flux. When the sacks have different y-positions the flux is reduced in order to prevent excess mixing resulting from an overestimate of $|\partial q/\partial x|$ (i.e., the difference

in q for the two sacks is also proportional to $\partial q/\partial y$ in this case). The flux in the y-direction is calculated in a similar way, except, of course, sacks are partitioned into sections parallel to the y-axis. The tendency of q for a given sack is as follows:

$$\frac{dq}{dt} = \frac{1}{M_i} \left(Q_{i-1/2} - Q_{i+1/2} + Q_{j-1/2} - Q_{j+1/2} \right) \tag{17}$$

where i (j) indicates the sack's position in its x-section (y-section). In order to implement horizontal viscosity, (16) and (17) are applied to each component of velocity independently. Momentum fluxes at the horizontal boundaries are set to zero for the free-slip boundary condition, and a virtual motionless sack is included at the boundary for a no-slip boundary condition.

While this formulation of horizontal diffusion is only an approximation of its counterpart in a finite-difference model, tests suggest that it mixes momentum and/or tracers in a similar way. For example, Fig. 3 shows a case in which a tracer having an initial Gaussian distribution with an amplitude of 1 and a radius of 0.1 is mixed for 10 time units in a finite-difference model (Fig. 3a) and in the slippery sacks model (Fig. 3b) given $v = 0.001$ (all variables are non-dimensional). For the latter case the domain is divided into 20 sections in both the x- and y-mixing calculations. In both cases the maximum tracer concentration is reduced by a factor of about 5 (Fig. 3a and b). Moreover, the tracer spreads to cover a similar area in the two simulations. This experiment was also conducted with 10 and 40 mixing sections, and in each case the resulting field at $t = 10$ differed from that for the 20-section case by about 18%, suggesting that the scheme is sensitive to the number of divisions used, but not drastically so. We also tried rotating the diffusion rows and columns 45° (Fig. 3c), and while individual tracer values changed slightly, the overall distribution remained close to that for the finite difference simulation (Fig. 3a).

For the simulations of homogeneous oceans presented later in the paper the number of mixing sections is set to the number of sacks in a row or column in the initial sack array. This equates to using mixing columns and rows that are 1/3 to 1/5 of a sack radius wide. A minimum distance of 0.005–0.01 between adjacent sacks is assumed for the flux calculation in order to ensure numerical stability. For the three-dimensional simulation presented in Section 6 we use mixing columns and rows that are a sack radius wide.

3.2. Horizontal mixing in three-dimensional simulations

Above we describe how the horizontal mixing scheme is applied to a single layer of sacks. The scheme is applied in three-dimensional oceans by first partitioning sacks into layers, and then applying the scheme to one layer at a time. For the three-dimensional simulations presented below we tried partitioning sacks according to their height (producing mixing along z-surfaces) and according to their density (producing isopycnal mixing). The two methods produced similar results, and we elected to present simulations with isopycnal mixing, which more realistically represents horizontal mixing by eddies. Note that even in three-dimensional oceans the mixing scheme requires $O(n)$ operations to complete[5] where n is the number of sacks. One pass through the sacks is made to assign them to layers, x-rows, and y-rows, and then another pass through each row to do the mixing between adjacent sacks.
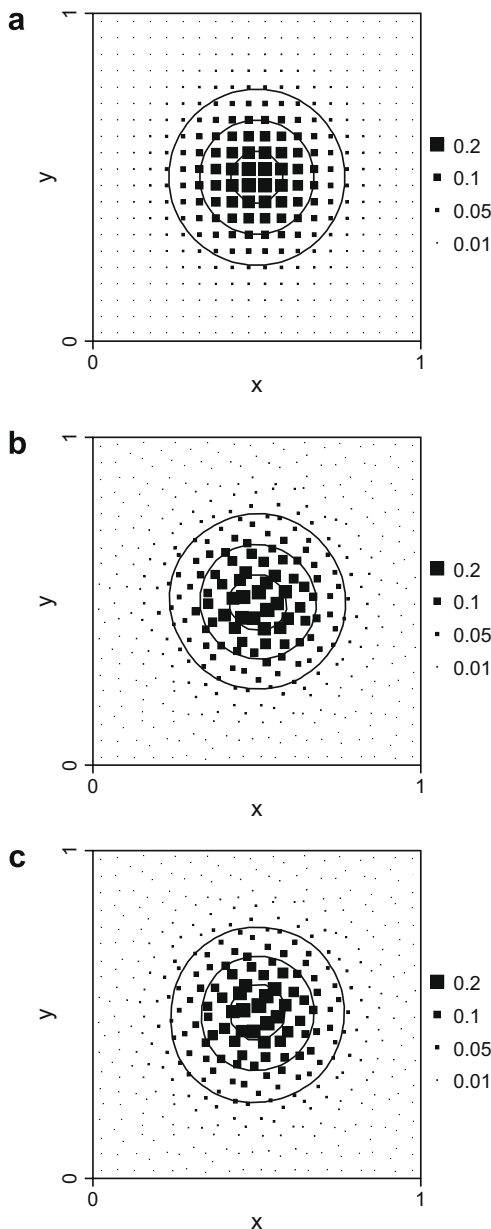

Fig. 3. A test of the horizontal mixing scheme. In each panel a box is plotted for each grid point or sack, and its size indicates the tracer value. Tracer values at $t = 10$ for (a) the finite difference simulation, (b) the slippery sacks simulation with diffusion rows and columns parallel to x- and y-axis, and (c) the slippery sacks simulation with diffusion rows and columns rotated 45°. Contours are plotted for tracer values of 0.05, 0.1, and 0.15.

---

[5] Even though the sorting of sacks by position is required for the mixing scheme, which is an $n \log(n)$ operation, in practice, when resolution is increased the sizes of sub-domains for parallel processing are decreased as are row/column sizes so that the number of sacks that needs to be sorted remains about constant for each row/column. Moreover, this sorting accounts for a small percentage of the computations in a time step.

4. Potential energy barriers to circulating slippery sacks

While carrying out simulations of western boundary currents in homogeneous oceans we encountered an interesting phenomenon: in order for non-divergent circulations to develop in an initially motionless pile of slippery sacks, the system must escape a potential energy well. If the forcing applied to the system is too weak, the sacks oscillate weakly about their initial positions rather than circulating. Fortunately, there are ways to reduce the potential energy barrier to circulations to mitigate its adverse impacts on simulations. In this section we illustrate the potential energy barrier concept, first for a simple system with a single slippery sack, and then for a slippery sacks representation of a homogeneous ocean.

4.1. The lone sack in a valley

Suppose a slippery sack is initially motionless, sitting in a valley in a region with sinusoidal topography (Fig. 4a). Let A denote the amplitude of the topographic variations and L denote their length scale. Suppose also that a steady force τ is applied to the sack in the positive x-direction (e.g., from a wind stress), and that once the sacks starts moving this force is opposed by a frictional force $-kuM$ where k is the velocity damping coefficient, u is the sack's horizontal velocity, and M is the sack's mass. Assuming that the sack's radius is small compared to L, the equation of motion for the sack is as follows:

$$\frac{du}{dt} = \frac{\tau}{M} - g\frac{\partial b}{\partial x} - ku \qquad (18)$$

where b is the height of the bottom topography and g is gravity. We now consider how solutions to this equation vary as A is increased from zero. We assume the sack is initially motionless and that $\tau/m = 1\ \mathrm{ms}^{-2}$, $k = 0.1\ \mathrm{s}^{-1}$, and $L = 2\pi m$. The solutions are approximated using forward time-differencing with a time step of 0.01 s.

We first consider the case $A = 0$ (flat topography). Initially, the forcing dominates the frictional dissipation and the sack accelerates at a rate of almost τ/M (1 ms^{-2}). Later the frictional acceleration approaches $-\tau/M$, and the sack's velocity approaches a constant value of $\tau/(Mk) = 10\ \mathrm{ms}^{-1}$ (Fig. 4b). Now suppose $A = 0.05$ m. In this case the sack is in a small potential energy well. However, the forcing provides more than enough energy to escape, and the sack's velocity is quite similar to that in the $A = 0$ case differing only by small perturbations at later times (Fig. 4b) that result from ascending and descending hills. The solution is drastically different when A is increased to 0.15 m, however. The potential energy well is sufficiently deep that the sack does not escape, and it moves back and forth within the valley with velocity perturbations about an order of magnitude smaller than those in the $A = 0$ case (Fig. 4b). Further increasing A to 0.2 m results in similar oscillatory behavior, but with a higher frequency (Fig. 4b).

4.2. Multiple sacks in a basin

An analogy may be drawn between the above problem and the problem of how a steady wind stress stirs up a circulation in a slippery sacks representation of our homogeneous ocean. It turns out that solutions to the latter problem have a similar character to those to the former problem. Namely, there is a potential energy barrier that must be overcome before a quasi-steady circulation develops in the pile of sacks, or else the sacks oscillate weakly about their initial positions. We illustrate this point by comparing slippery sacks simulations to an analytic solution of a simplified version of (1) and (2).

(1) Linear solution.
    Since the potential energy barrier is unrelated to the Coriolis force, we neglect it to simplify solutions (i.e., we neglect the
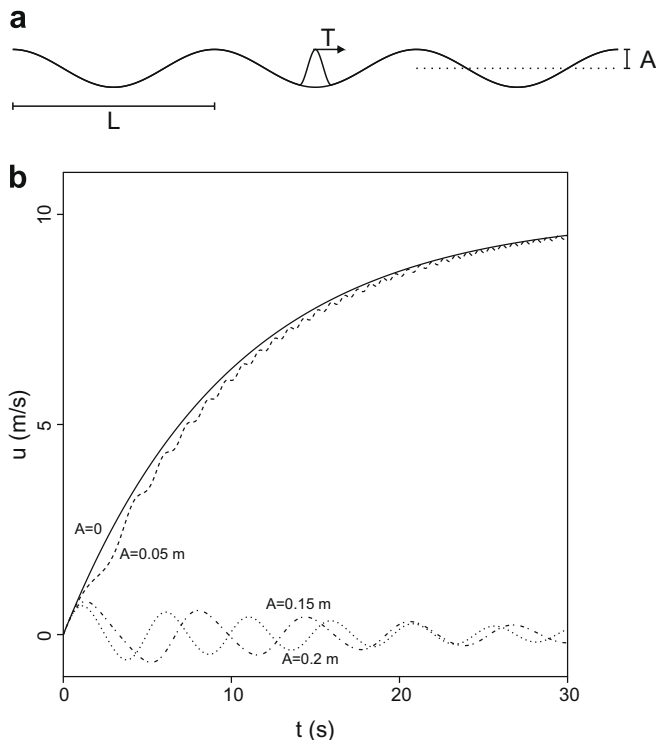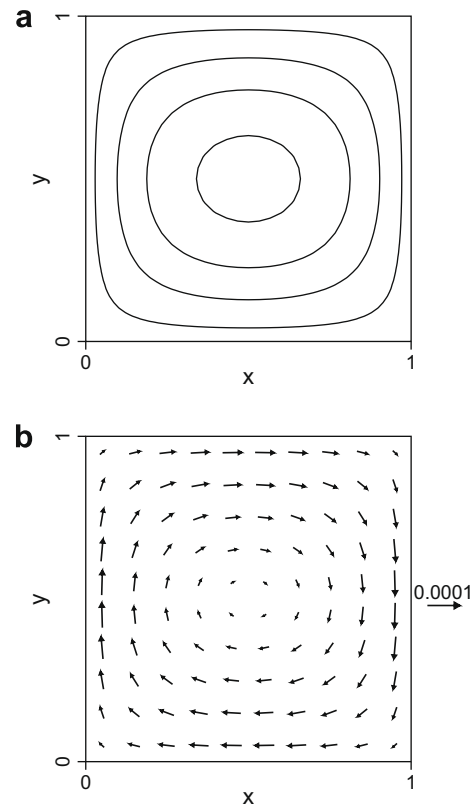

Fig. 4. The lone slippery sack in a valley. (a) Schematic. (b) Velocity as a function of time for different values of the topography amplitude A.

Fig. 5. The analytic solution for the homogenous ocean in a non-rotating frame of reference. (a) Stream function (contours: $\psi = 2.5 \times 10^{-6}, 7.5 \times 10^{-6}, 12.5 \times 10^{-6}, 17.5 \times 10^{-6}$). (b) Velocity vectors.

third term on the right hand side of (1)). If we also neglect viscosity, then the steady solution to (1) and (2) is as follows:

$$\psi = \frac{\tau_0}{k\pi} \sin(\pi y) \left[1 - \cosh(\pi x) + \frac{\cosh(\pi) - 1}{\sinh(\pi)} \sinh(\pi x) \right] \qquad (19)$$

The forcing generates a broad anticyclonic gyre that is symmetric in the east-west and north-south directions (Fig 5a). Fig. 5b shows the amplitudes of velocities for $\tau_0 = 10^{-5}$ and $k = 0.1$ for comparison with slippery sacks simulations presented below.

(2) Slippery sacks solutions.

For the first simulation we use a non-dimensional gravity $\tilde{g} = 0.16$, which corresponds to using a realistic value of gravity for a 5 km deep ocean. We represent our ocean with a 10 by 10 array of sacks with an overlap parameter of 1 (i.e.,

a cross-section of the pile aligned with a row of sack centers looks like Fig. 2b). At first the sacks begin rotating anticyclonically (Fig. 6a) mimicking the circulation shown in the analytic solution (Fig. 5). However, this motion does not persist long, and by $t = 6$ a cyclonic gyre has developed (Fig. 6b). With time the circulation oscillates between cyclonic and anticyclonic and weakens (not shown). Note that the magnitude of the circulation is about an order of magnitude smaller in the pile of sacks than in the analytic solution (compare the vector amplitudes in Figs. 5b and 6a and b). The simulated circulation is reminiscent of the oscillation of the lone slippery sack in a valley when the wind stress does not impart enough energy for the sack to escape the potential energy well (Fig. 4b, $A = 0.15$, 0.20 m cases). Moreover, the same physical reasoning may be used to interpret the oscillating gyre. In their initial state the pile of sacks
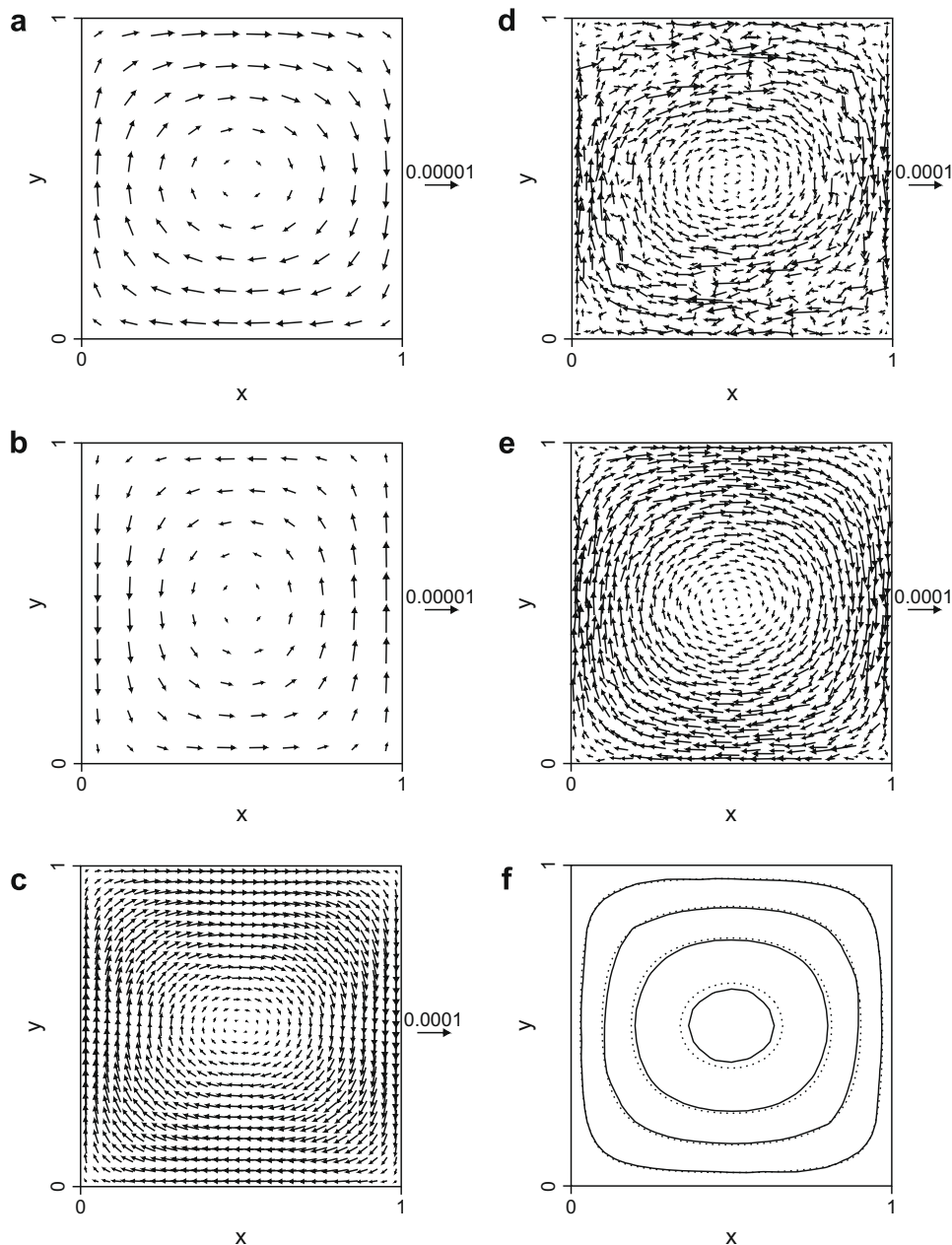

Fig. 6. Slippery sacks simulations of the homogenous ocean in a non-rotating frame of reference. (a) Velocity vectors for a sack overlap of 1 at $t = 2$. (b) Velocity vectors for a sack overlap of 1 at $t = 6$. (c) Velocity vectors for a sack overlap of 3 at $t = 100$. (d) Velocity vectors for a sack overlap of 3 at $t = 10,000$. (e) Velocity vectors for a sack overlap of 3 with $g = 0.001$ at $t = 50,000$. (f) simulated (solid) and analytic (dotted) stream functions for a sack overlap of 3 and $g = 0.001$ at $t = 50,000$ (contoured as in Fig. 5a).

has a perfectly level free surface which corresponds to the minimum potential energy state of the system. When the sacks begin rotating, even if their velocity vectors are non-divergent, it is inevitable that bumps and pits will develop in the free surface of the pile, which correspond to a higher potential energy state. Evidently, the energy imparted by the wind stress is not sufficient for the system to escape the potential energy well, so the sacks oscillate weakly, maintaining their initial positions in the array. Moreover, when gravity is reduced slightly and the simulation is repeated, the circulation oscillates with a lower frequency, which is consistent with the potential energy well interpretation.

One way to reduce the potential energy barrier is to use thinner sacks that have a greater degree of overlap. For example, suppose we represent the ocean with a 30 by 30 array of sacks with an overlap parameter of 3. Note that the sacks have the same radius as before, but are now 9 times as thin (see Fig. 3b–d for an illustration of increasing sack overlap, but note that in the three-dimensional case the reduction in sack vertical thickness is proportional to the square of the overlap parameter). When these sacks begin to rotate around the basin, smaller pits and bumps develop in the free surface, and there is a smaller potential energy well for the system to escape. When the sacks are exposed to the wind stress, a persistent, strong anticyclonic circulation develops that is very much like the analytic solution (Fig. 6c). However, this circulation is not completely steady. At later times, when sacks have departed significantly from their initial positions, small-scale variability develops as well (e.g., Fig. 6d). If the steady solution were unstable, we would expect such variability to spontaneously develop from a theoretical viewpoint (e.g., Sheremet et al., 1997; Sheremet, 2002). However, in this case the damping is very strong making it likely that the linear steady solution is stable. Rather, it appears that the variability is caused primarily by local potential energy barriers to sacks crossing over another that deflect sacks paths from analytic streamlines. Tests show that the variability can be reduced in three ways: (1) by decreasing gravity (or using gravity wave retardation in three-dimensional simulations); (2) by using thinner sacks, and (3) by including viscosity. For example, Fig. 6e shows that when we repeat the simulation depicted in Fig. 6d using $\tilde{g} = 0.001$ the small-scale variability is much weaker, even after running the model out to $t = 50{,}000$. Alternatively, increasing the sack overlap parameter to 5 and using a viscosity $v = 1.25 \times 10^{-4}$ reduces the noise and produces a simulation of comparable quality (not shown). For the simulations presented later in this paper we use a combination of these approaches to control small-scale variability.

Since the figures containing sack velocities for every sack (e.g., Fig. 6e) are busy and often difficult to compare with analytic solutions, for many simulations presented in the remainder of the paper we compare simulated and analytic stream functions. For example, Fig. 6f is such a plot that corresponds to the sack velocities shown in Fig. 6e. Note that both the simulated and analytic solutions use the same contour values, allowing for a careful comparison of both the flow patterns and the amplitude of the circulation. In this case the flow patterns are quite similar, and contours for the simulation lie just inside those for the analytic solution, meaning that the simulated circulation is slightly weaker than the analytic solution.

5. Simulations of western boundary currents

In this section we present simulations of the Stommel and Munk solutions conducted with the SSOM. The purpose for carrying out these simulations is to test the model's ability to generate wind-forced gyres whose structures depend on either lateral or bottom friction. Most of the simulations are in linear regimes,

Table 1
Simulations of the Stommel solution.

Simulation name	τ_0	k	Radius	g	Overlap
Low-resolution	10^{-5}	0.05	0.1	0.001	3
Medium-resolution	10^{-5}	0.05	0.05	0.0005	5
Moderately non-linear	3.2×10^{-5}	0.01	0.025	0.0005	5

and these are compared with analytic solutions. We also present two simulations that are moderately non-linear.

5.1. Simulations of the Stommel solution

Parameter values for simulations of the Stommel solution are listed in Table 1. The simulations include low- and medium-resolution runs in linear regimes, and a moderately non-linear simulation. In all cases we use a low value for gravity and a sack overlap parameter of at least 3 to minimize problems associated with potential energy barriers to sacks crossing one another.

As a starting point, we test the SSOM's ability to reproduce the Stommel solution for $k = 0.05$ with relatively large sacks. We use a sack radius (0.1) that is actually twice the theoretical boundary current width (k).[6] Only 900 sacks are used for this simulation, which allows velocity vectors to be plotted for every sack making the behavior of individual sacks easy to discern. A quasi-steady circulation develops with a western boundary current that has roughly the same width and amplitude as that predicted by linear theory (e.g., Fig. 7a). While there is some evidence of chaotic behavior, especially in the upper-left quadrant, the time-averaged stream function has a similar structure to that for the linear solution (Fig. 7b). The circulation is a bit weaker than predicted with a maximum value for the simulated stream function that is 8% lower than that for the analytic solution. However, considering that the theoretical current is under resolved, this is not a discouraging result. Moreover, when narrower, thinner sacks are used the SSOM simulation becomes more like the analytic solution (Fig. 7c). Due to the fact that the SSOM is actually modeling a different physical system (with sloping walls and a free surface) than that to which the analytic solution applies, we do not expect a precise reproduction of the analytic solution, nor do we attempt to discern a rate of convergence. However, we do consider the qualitative behavior of the SSOM in a moderately non-linear regime. By reducing k to 0.01 and increasing τ_0 to 3.2×10^{-5} we increase the scale of the inertial boundary layer to be equal to that of the Stommel boundary layer, which should enhance the relative importance of non-linear terms. Fig. 7d shows that as expected the model produces a narrow and intense western boundary current, which continues along the northern boundary for a time. This figure closely resembles Fig. 6 in Veronis (1966), which is a simulation of the Stommel solution in a similar parameter regime. In particular, both simulations exhibit the "looping" of streamlines in the northwest corner of the basin, which is the primary departure from the linear solution.

5.2. Simulations of the Munk solution

In the simulations of the Stommel solution, the linear velocity damping coefficient k determines the width of the western boundary current. In this section we set $k = 0$ and model western boundary currents whose widths depend on the horizontal viscosity coefficient v. Once again we conduct low- and medium-resolution simulations in linear regimes, and we explore the qualitative

---

[6] Note that because the horizontal mixing scheme essentially treats sacks as points, it is actually possible to simulate circulations narrower than a sack radius with the SSOM.
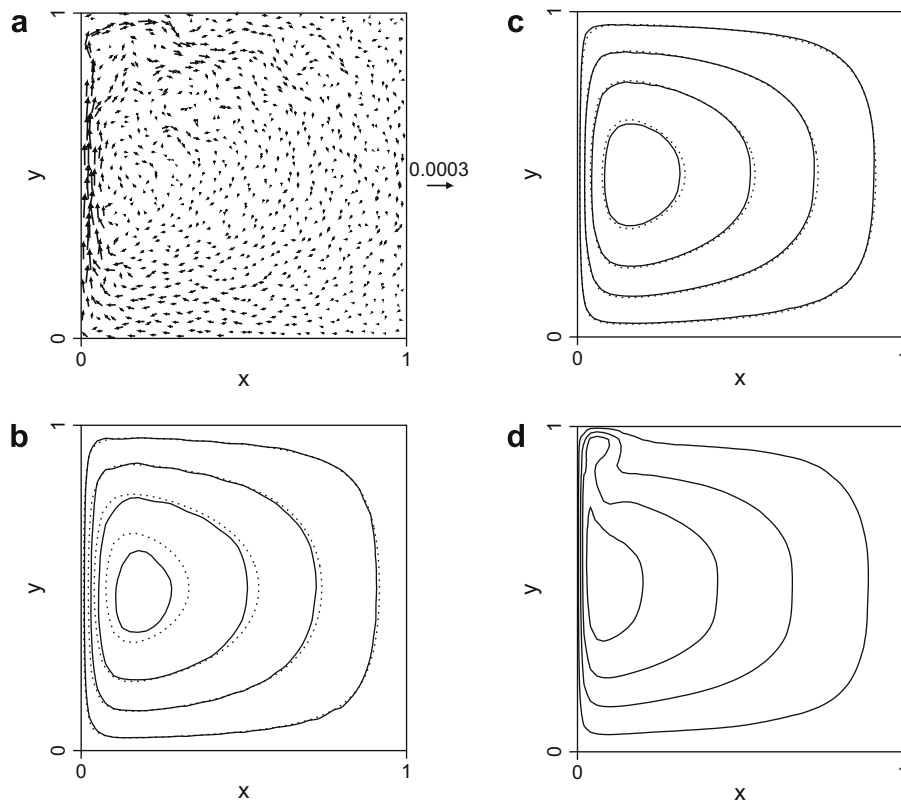
Fig. 7. Simulations of the Stommel solution. (a and b) Sack velocities and stream function for the low-resolution simulation. The simulated (solid) and analytic (dotted) stream functions are contoured as in Fig. 1a. (c) Stream function for the medium-resolution simulation (contoured as in (b)). (d) Stream function for the moderately non-linear Stommel simulation (contours: $\psi = 6 \times 10^{-6}, 18 \times 10^{-6}, 30 \times 10^{-6}, 42 \times 10^{-6}$).

Table 2
Simulations of the Munk solution.

Simulation name	τ_0	ν	Radius	g	Overlap
Low-resolution	10^{-5}	1.25×10^{-4}	0.1	0.001	3
Medium-resolution	10^{-5}	1.25×10^{-4}	0.05	0.0005	5
No-slip	10^{-5}	1.25×10^{-4}	0.05	0.0005	5
Moderately non-linear	3.2×10^{-5}	1×10^{-6}	0.025	0.001	3

behavior of the model in a moderately non-linear regime. While most of the runs employ a free-slip boundary condition (as in our simulations of the Stommel solution), we also carry out one simulation with a no-slip boundary condition. For most of the runs we use $\nu = 1.25 \times 10^{-4}$, which, according to linear theory, should produce a boundary current with a non-dimensional width of $\delta_m = 0.05$. The model parameters other than ν and k are the same as those used in the Stommel runs (Table 2).

The low-resolution version of the model produces a western boundary current whose width and intensity are approximately consistent with theory (Fig. 8a). The circulation is quasi-steady, and, apart from some small-scale variability and some meandering of the northern-quarter of the boundary current, it changes little once the initial adjustment has occurred. The small-scale variability is weaker in this case than in the Stommel runs (e.g., compare Figs. 7a and 8a), presumably because horizontal viscosity selectively damps small-scale flow features. The time-averaged stream function is plotted in Fig. 8b along with the analytic streamlines. The two solutions have similar flow patterns, but the slippery sacks solution (solid lines) has a weaker gyre and western boundary current. The maximum value of ψ for the simulation is 15% less than that for the analytic solution. Considering that the sack radius (0.1) is twice the Munk boundary layer scale (0.05), it is not surpris-

ing that the model produces a weaker circulation than the theory predicts (i.e., the western boundary current is under resolved). Some other factors that could contribute to this discrepancy include the implementation of horizontal diffusion, sloping topography near the boundaries, mixing by small-scale variability, and the fact that model has a free surface. When thinner and narrower sacks are used, the simulated circulation becomes more like the analytic solution (Fig. 8c). The fidelity of SSOM solutions to analytic solutions does not seem particularly sensitive to the choice of boundary condition; Fig. 8d shows the flow pattern for a run with the no-slip boundary condition. Overall, the performance of the model is similar to that for the corresponding free slip simulation (Fig. 8c) with an amplitude difference of a few percent from the analytic solution.

The Munk simulations discussed above are for parameter regimes that are only weakly non-linear. We now adjust parameters so that non-linear effects become more significant, as we did for the Stommel simulations. By reducing ν and increasing τ_0 we increase the scale of the inertial boundary layer to be the same as that of the Munk boundary layer, which should enhance the relative importance of non-linear terms. Fig. 8e shows that as expected the model produces a more narrow and intense western boundary current. Other differences from linear simulations include the continuation of the boundary current along the northern boundary, and the presence of a recirculation gyre in the northwest corner of the basin. These features have been noted in previously pub(e.g., Bryan, 1963; Ierley, 1987).

6. Building an idealized model of the North Atlantic Ocean

Taking advantage of the new horizontal mixing scheme and using what we have learned from experiments with homogeneous oceans, we now build an idealized model of the North Atlantic
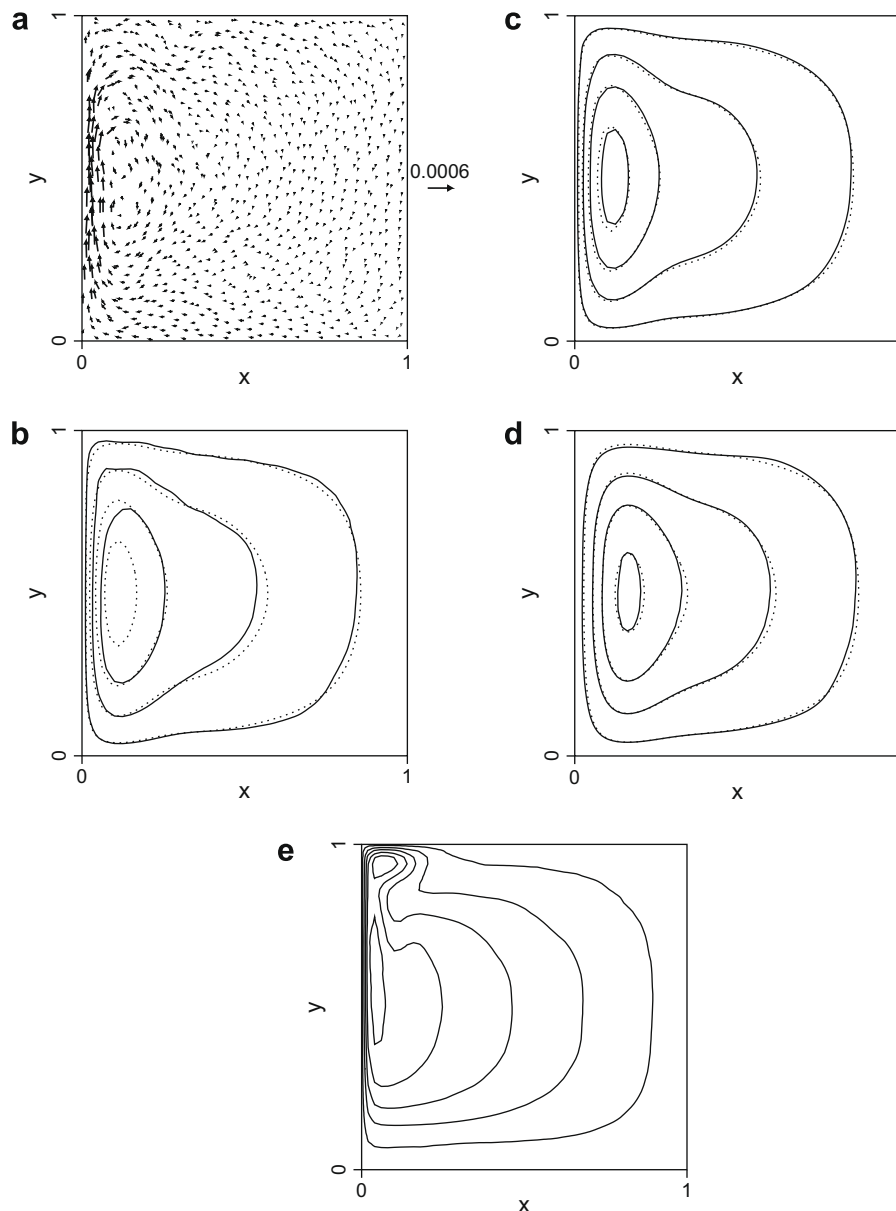
Fig. 8. Simulations of the Munk solution. (a and b) Sack velocities and stream function for the low-resolution simulation. The simulated (solid) and analytic (dotted) stream functions are contoured as in Fig. 1b. (c) Stream function for the medium-resolution simulation (contoured as in (b)). (d) The simulated (solid) and analytic (dotted) no-slip Munk solutions (contours: $\psi = 4, 12, 20, 28 \times 10^{-6}$). (e) The moderately non-linear Munk simulation (contours: $\psi = 1, 3, 5, 7, 9, 11, 13 \times 10^{-5}$).

Ocean with the SSOM. We actually have two purposes for developing this model: (1) to test the SSOM's ability to simulate wind-forced gyres and overturning in a more complicated and realistic setting; and (2) to prepare the SSOM for studies of meridional over-turning, oceanic heat transport and the carbon cycle. We compare simulations conducted with the SSOM to similar simulations carried out with the Massachusetts Institute of Technology general circulation model (MITgcm), but which are run at a much higher-resolution. Our goal is to reproduce the basic temperature and circulation structure the occurs in the MITgcm in a much lower-resolution version of SSOM that can be run on a small desktop or laptop computer.[7] We also explore how circulations change in

the limit of no tracer diffusion, an exercise for which the SSOM is well suited.

6.1. The ocean and its forcing

The ocean and forcing we use are similar to those used by Follows et al. (2002) to study the solubility pump of CO_2 in the subtropical oceans. The ocean is bounded by the 60° W and 0° E longitude lines, and by the 21° S and 69° N latitude lines, and it is 4500 m deep. The wind stress forcing and restoring function for temperature are shown in Fig. 9. They are both analytic approximations of National Center for Environmental Prediction reanalysis along 40 W for December through February 1968–1996. We use an equation of state that is a linear function of temperature:

$$\rho = \rho_0(1 - \alpha T)$$

---

[7] The North Atlantic simulations presented in this paper were run on a Mac Mini with a 2 GHz 65 nm Core 2 Duo CPU.
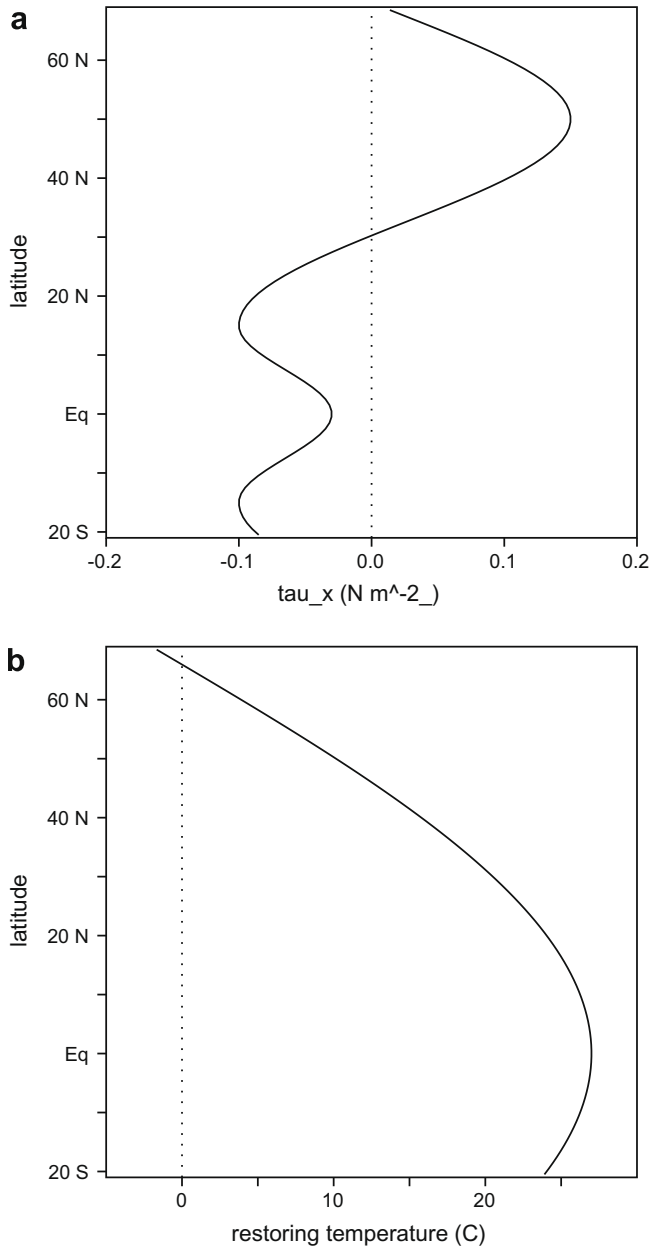
a

b

Fig. 9. The forcing used for North Atlantic simulations. (a) Zonal component of surface wind stress (the meridional component is zero). (b) Restoring temperature. Both the wind stress forcing and the restoring temperature are independent of longitude.
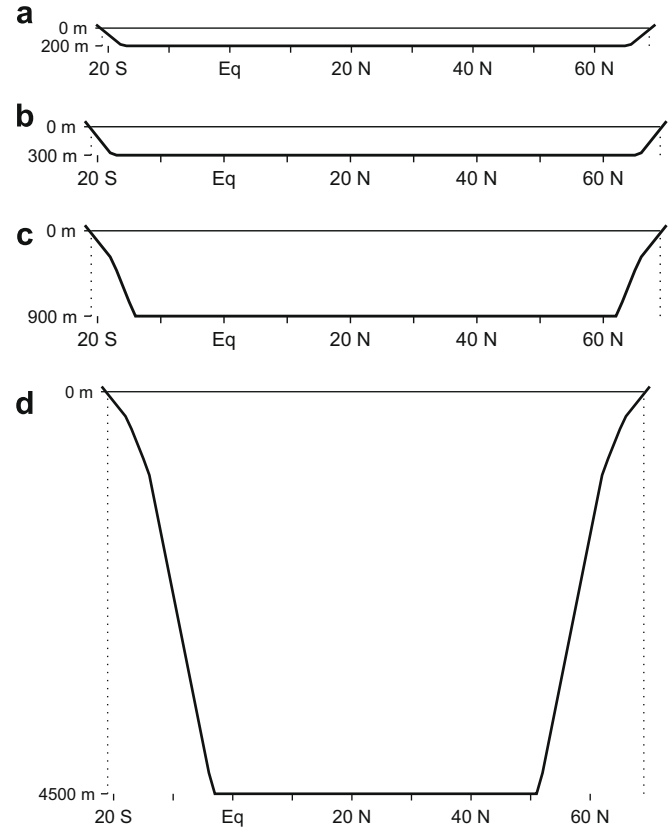

Fig. 10. North-south vertical cross-sections of basins used for preliminary North Atlantic simulations. (a) 200 m deep, (b) 300 m deep, (c) 900 m deep, and (c) 4500 m deep oceans.

where $\rho_0 = 1000$ kg m^{-3}, $\alpha = 0.0002$ K^{-1}, and T is temperature in degrees Celsius. The surface heat flux H is proportional to the difference between the average temperature of the upper 25–30 m T_s and the restoring temperature T_r:

$$H = H_0(T_s - T_r)$$

where $H_0 = 50$ Wm^{-2}K^{-1}. Both heat fluxes and wind stress forcings are distributed over the upper 25–30 m. The initial ocean temperature is a constant 2 °C. We use a horizontal viscosity of 10^5 m^2 s^{-1} (i.e., Munk boundary layer width of about 2° longitude), and a vertical viscosity of 10^{-3} m^2 s^{-1}. Vertical tracer diffusion is a constant 5×10^{-5} m^2 s^{-1} following Follows et al. (2002), and horizontal tracer diffusion is set to zero. The time step is 3600 s. We conduct simulations with two resolutions: (1) for comparisons of SSOM results and MITgcm results we use sacks with a 3° radius in both latitude and longitude; and (2) for the study of the effect of removing tracer

diffusion we use a sack radius of 4°. In both cases we use a sack overlap parameter of 3 when initializing layers. However, the sacks are more or less randomly distributed by the end of the simulations (after 300 years for the 3° run, and 700 years for the 4° run).

We developed the basin geometry in stages that represent a transition from the parameter regime of the non-dimensional simulations to one suitable for the Atlantic Ocean (Fig. 10). We started with shallow oceans (e.g., Fig. 10a), and we reduced the external pressure gradient by a factor of about 12 (GWR parameter of $\gamma = 0.08$; H04), which has the same effect on the potential energy barrier to sacks circulating as the factor of 12 reduction in gravity used for the medium-resolution Munk simulations presented in Section 5. Applying the forcing shown in Fig. 9 to this ocean yields a horizontal circulation pattern (Fig. 11a) similar to that produced by MITgcm (Fig. 11d), but with a stream function amplitude reduction on the order of 15%. This result is consistent with the results of the low-resolution non-dimensional Munk simulations (Fig. 8a and b and Table 2). We then made the ocean successively deeper, first by increasing the basin depth and the vertical thickness of each sack (Fig. 10b), and then by adding layers of even thicker sacks (Fig. 10c and d). We further reduced the GWR parameter, using values of 0.028, 0.014, and 0.007 for the oceans shown in Fig. 10b–d, respectively. Such reductions in γ allow the use of long time steps and they also reduce the potential energy barrier to circulating sacks (Section 4), which is necessary when both the vertical thicknesses of sacks are increasing, and the average amplitudes of sack velocities are decreasing as the ocean gets deeper. In all cases the gross structure of the horizontal flow is similar (Fig. 11a–c), but as the depth of the ocean increases regions of positive (negative) stream function near the western boundary are enhanced (reduced), because the southward component of deep overturning
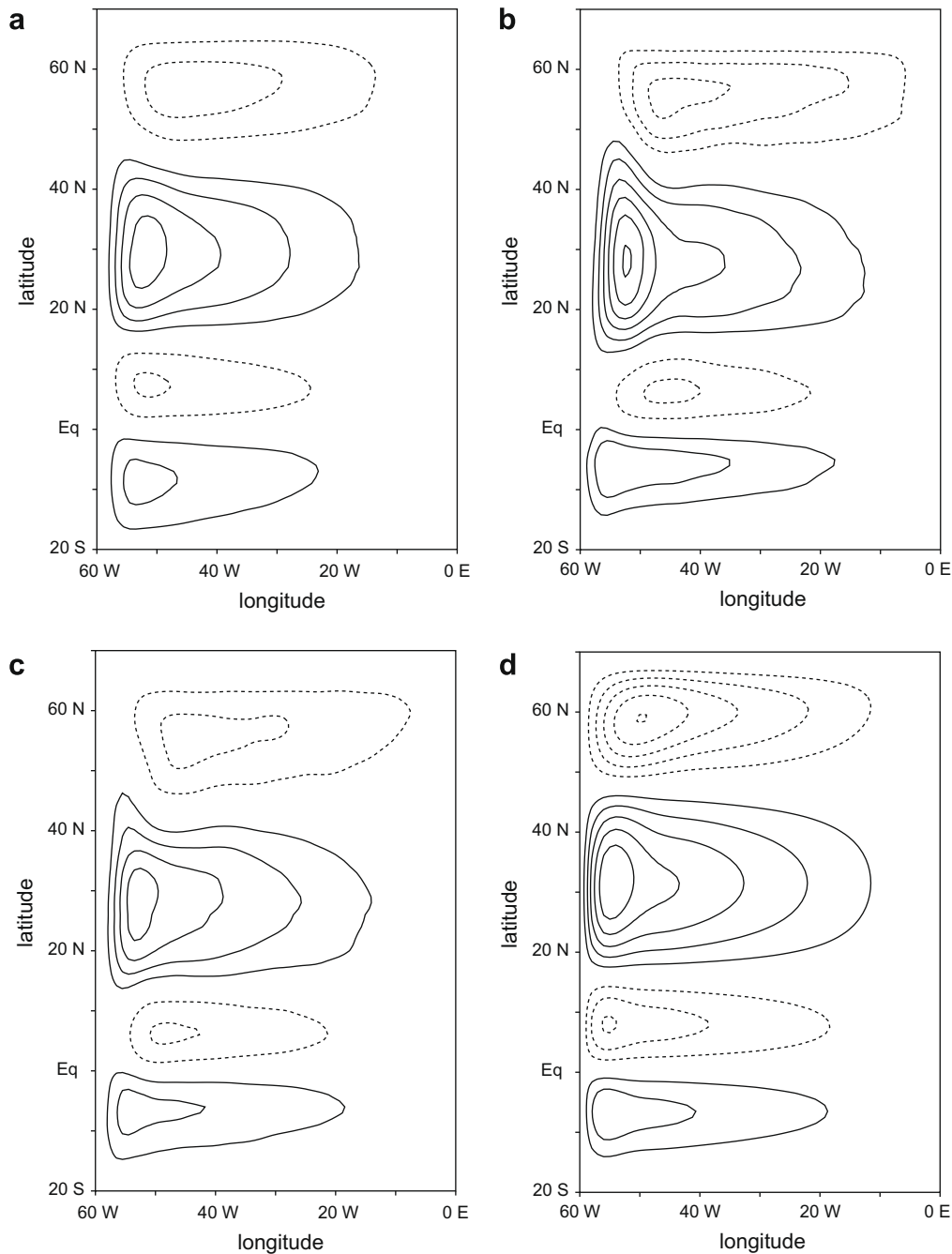
Fig. 11. Horizontal stream function (5 Sv contours) for (a) the 200 m deep ocean, (b) the 900 m deep ocean, (c) the 4500 m deep ocean, and (d) the MITgcm run.

(i.e., the deep western boundary current) is displaced eastward of the northward component. Note that one consequence of the using such gravity wave retardation is that surface height perturbations are amplified by a factor of $1/\gamma$.[8] For the ocean shown in Fig. 10d, the standard deviation in the free surface after 300 years of integration is 54 m. While these perturbations would be unacceptable for some applications, they do not have a large impact on the structure of the upper ocean, and a 1–2% change in the ocean depth is not serious side effect for our purposes. Moreover simulations conducted with less gravity wave retardation (e.g., $\gamma = 0.01, 0.014$) produced

very similar results (but required shorter time steps and more computations).

6.2. Spherical geometry

The form of spherical geometry suggested by H04 is used for this study. Sack radii are held fixed in terms of degrees latitude and longitude, so conservation of mass dictates that sacks become vertically thicker as they move northward. For the full-depth basin (Fig. 10d), sacks are on average about 33 m thick in the upper layer (0–300 m depth), 67 m thick in the middle layer (300–900 m depth), and 100 m thick in the lower layer (900–4500 m depth). Sack masses are quantized (i.e., are integral multiples of 3.06×10^{15} kg), and a target mass quantum number is set for each

---

[8] Note these free surface anomalies are expected from the equations being solved (i.e., are a physical side effect of using gravity wave retardation), and are not a direct artifact of sack thickness.
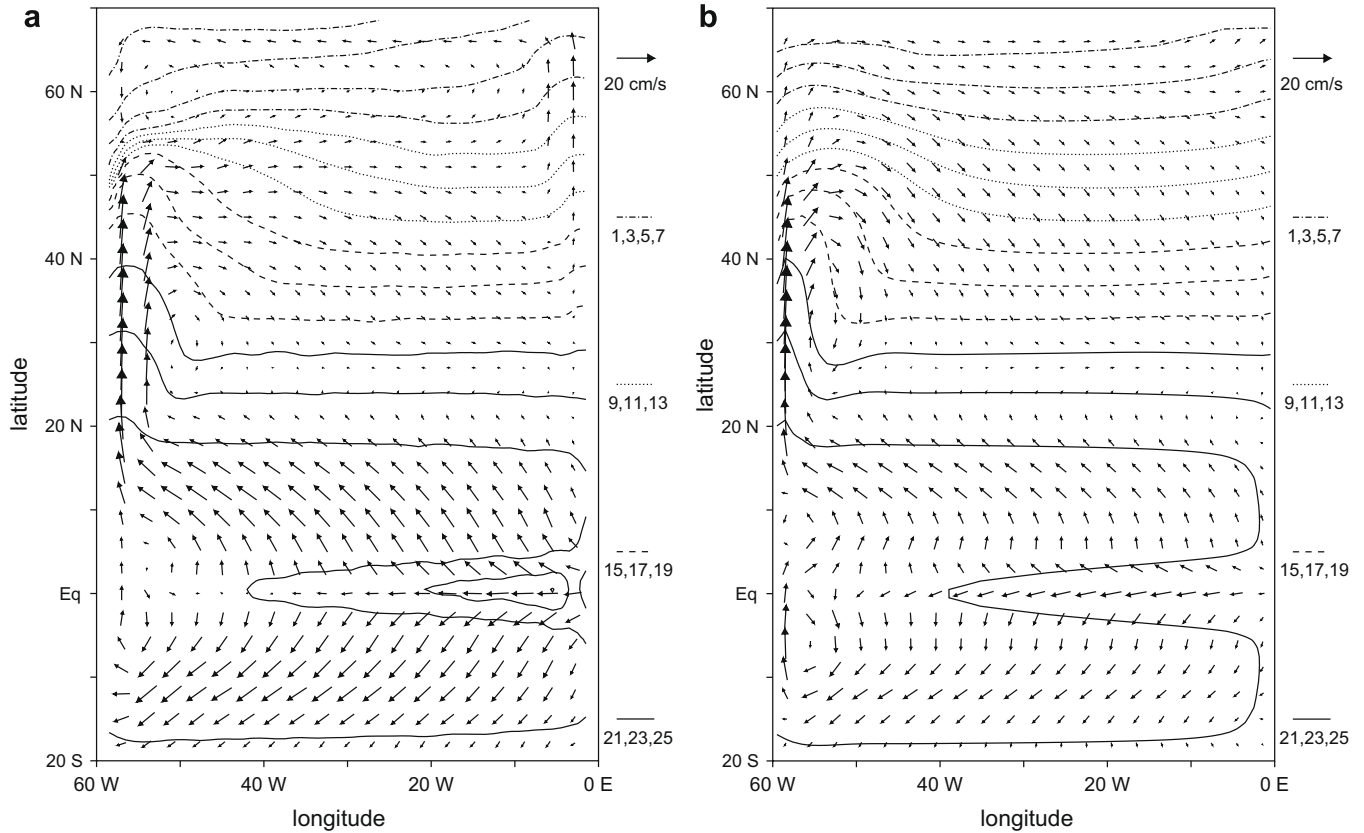
Fig. 12. Near surface temperatures and velocities. (a) SSOM. (b) MITgcm.

region: 1 in the upper layer, 2 in the middle layer, and 4 in the lower layer. As sacks enter regions with different target quantum numbers they are either sliced along their vertical midpoints or joined with nearby sacks to achieve the desired quantum number. While the joining of sacks introduces a small amount of mixing, this is contained by creating density classes and only allowing sacks in the same class to be joined together. One advantage of quantizing sack masses is that, even with dividing and merging sacks, individual mass elements can be tracked throughout the course of a simulation.

6.3. Comparing SSOM and MITgcm results

As noted above, the SSOM and the MITgcm produce wind-forced gyres with similar horizontal flow patterns (Fig. 11c and d). The surface fields produced by the two models are also similar (Fig. 12a and b). In both runs a western boundary current extends from about 15 N to about 50 N, and an equatorial cold tongue with westward flow extends from the eastern boundary to around 40 W. Not surprisingly, the MITgcm, which has three times the horizontal resolution of the SSOM, generates a narrower western boundary current (Fig. 12b). The vertical shear in the western boundary current, and the east-west slope of the thermocline are also similar in the two models (Fig. 13a and b), although the water is slightly cooler near the western boundary around 800 m in the SSOM (Fig. 13a and b). The most notable differences in the meridional flow are the fact that the return flow in the SSOM is weaker and farther eastward, which is probably attributable to the lower horizontal resolution (Fig. 13a and b).

Even at very low-resolution, the SSOM is able to produce a north-south temperature pattern quite similar to that generated by MITgcm (Fig. 14a and b). Not only is the thermocline shape
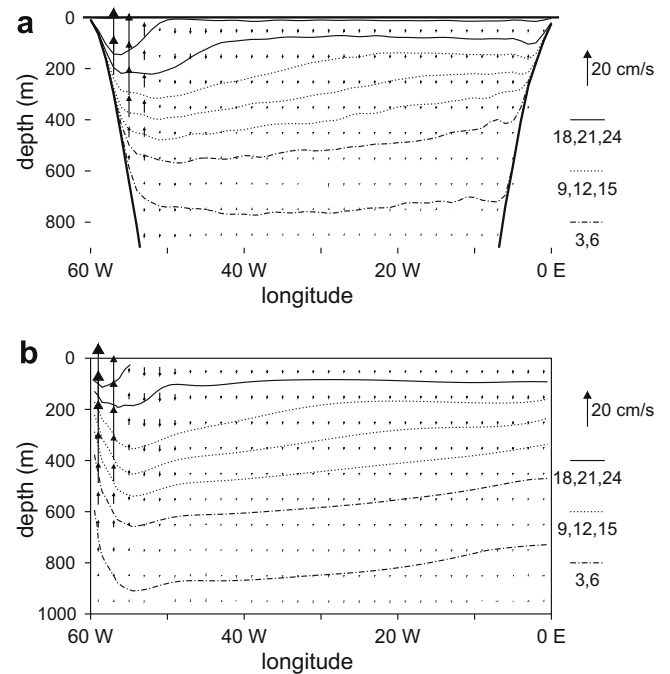

Fig. 13. Vertical cross-sections of temperature and meridional current along 30 N for (a) SSOM and (b) MITgcm. Upward vectors indicate northward flow.

and depth similar to that produced by the MITgcm, but also many of the individual temperature contours lie in similar positions in the upper 500 m. For example, the vertical spreading of the isotherms at the depth (∼100 m) of the equatorial undercurrent is reproduced in both models. The 3 C contour is somewhat deeper
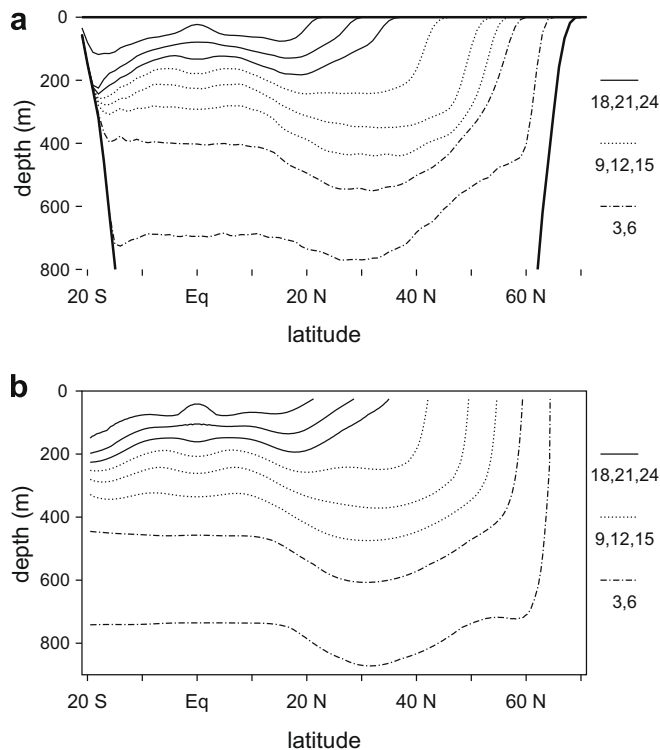
Fig. 14. Vertical cross-sections of temperature along 40 W for (a) SSOM and (b) MITgcm.
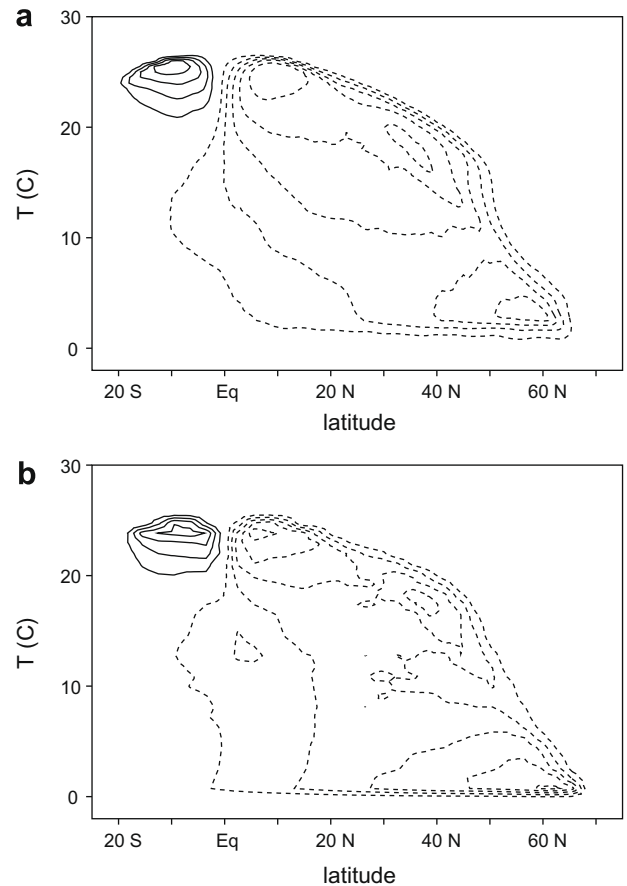

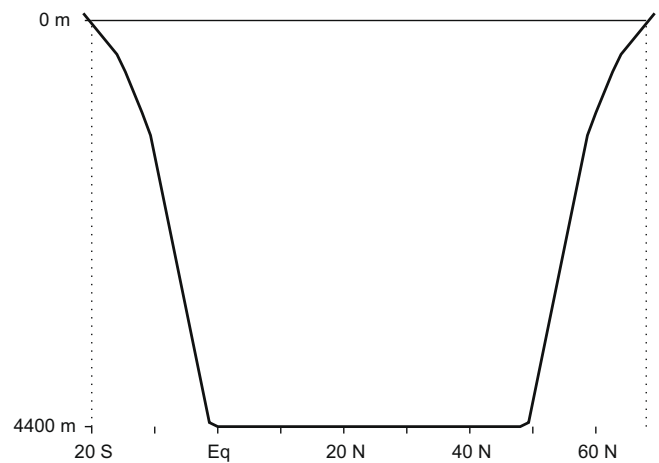**Fig. 15.** Meridional overturning (3 Sv contours) for (a) SSOM and (b) MITgcm.

Fig. 16. North-south vertical cross-section of the basin used to study the effects of removing tracer diffusion.

in the northern basin in the MITgcm run (Fig. 13b), but this more likely a consequence of differing basin geometry than of differing numerical approaches.

We compare the meridional overturning of the two models in temperature coordinates,[9] because the overturning structure is less sensitive to basin geometry in this coordinate system (Park and Bryan, 2000). Overall, the two models produce both shallow and deep overturning with a similar structure and amplitude (Fig. 15a and b). In both models there are upper equatorial cells with amplitudes of 12–15 Sv roughly 10° north and south of the equator at a temperature of about 24 °C. Similarly, midlatitude overturning cells with amplitudes in the range of 13–16 Sv occur around 38 N, 19 °C in both models. The greatest differences occur in the deep overturning cells centered near 58 N, 3 °C, which penetrate farther south in the MITgcm run (Fig. 15b). However, this difference could be largely a consequence of the differing basin geometries (Park and Bryan, 2000).

Overall, the comparison of SSOM and MITgcm runs for an idealized North Atlantic Ocean show that the SSOM produces reasonable temperature structures and circulation patterns, especially considering its relatively low-resolution.

6.4. Removing temperature diffusion

One unique feature of the SSOM is that it can be run without any tracer diffusion. In this section we compare SSOM runs that are identical except for the fact that vertical tracer diffusion is included in one, and it is set to zero in the other. We use a lower-resolution (4° sack radius, 44–188 m sack thicknesses) for these runs because they are extended to a longer period of time (700 years). We construct the basin in a similar manner as before, except that

the upper two layers are deeper, covering 0–400 m and 400–1200 m, respectively (Fig. 16). However, because of the greater sack radius the overall slope of the basin walls is similar (compare Figs. 10d and 16). We adjust the position of the meridional boundaries slightly to 20 S and 68 N in order to guarantee that there is a horizontal mixing row centered directly on the equator, and we also adjust the restoring temperature slightly to ensure the minimum restoring temperature occurring at the northern boundary is the same as before.
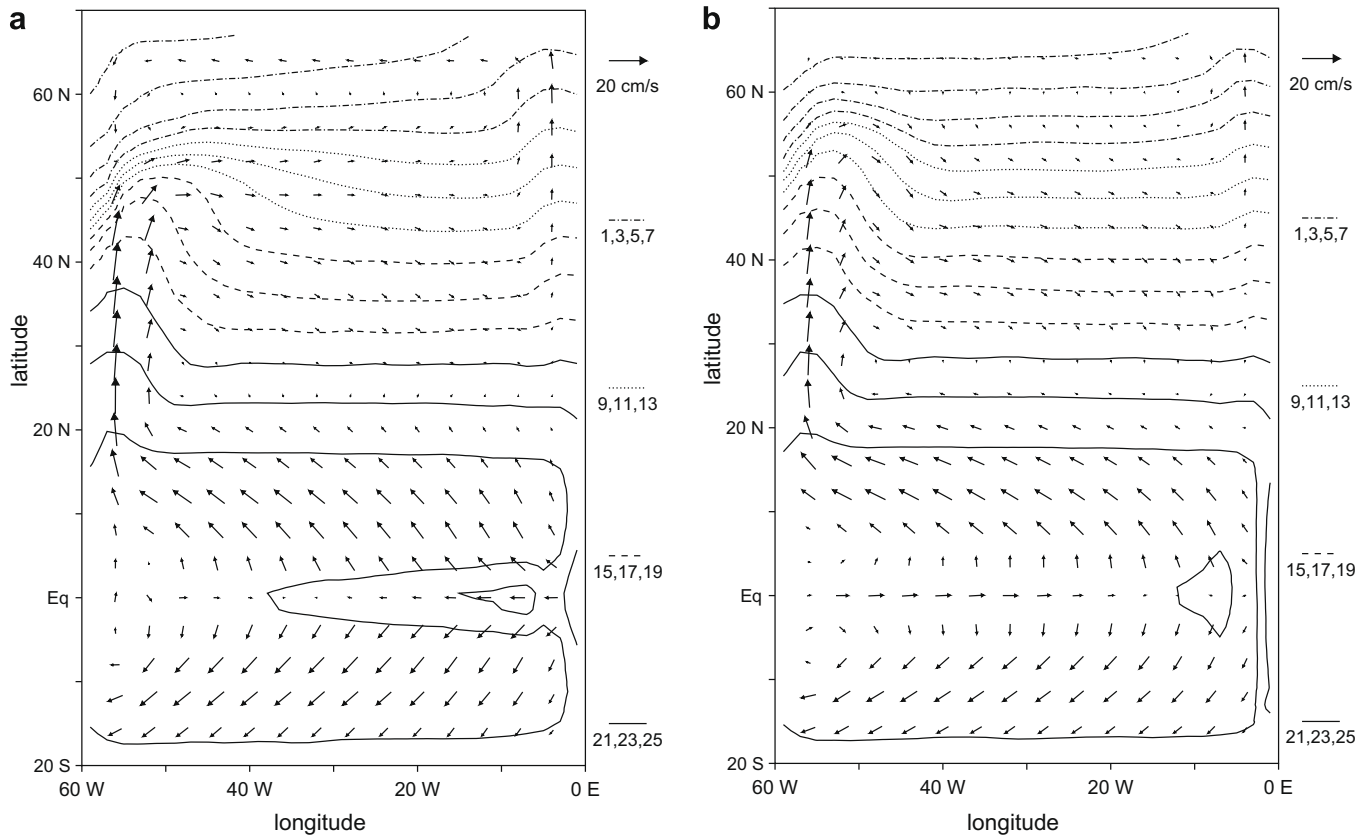
---

[9] Which is equivalent to using a density coordinate because density is a linear function of temperature.

Fig. 17. (a) Near surface temperatures and velocities for the lower-resolution SSOM run with tracer mixing. (b) Near surface temperatures and velocities for the lower-resolution SSOM run without tracer mixing.
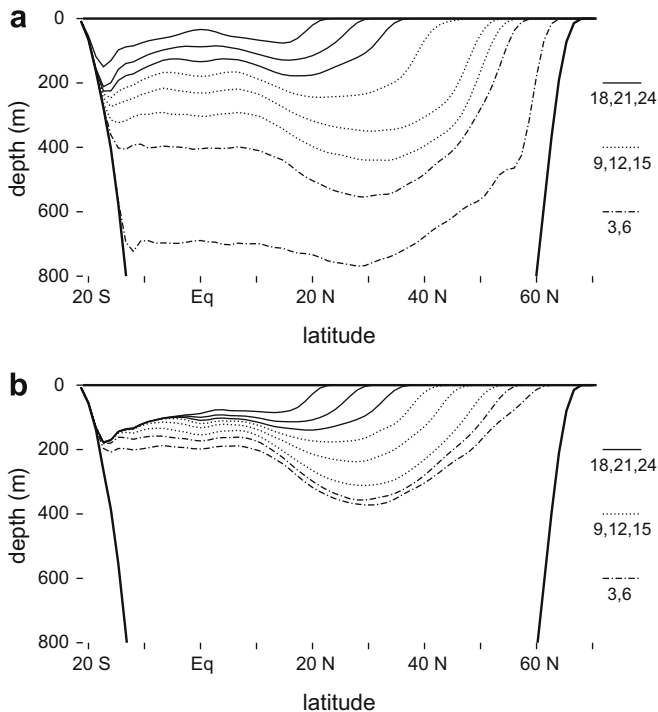

Fig. 18. Vertical cross-sections of temperature along 40 W for lower-resolution SSOM runs with (a) and without (b) tracer mixing.

Decreasing the resolution causes only minor changes in the gross surface, thermocline, and overturning structures (compare

Figs. 17a, 18a, 19a with Figs. 12a, 14a, and 15a, respectively). However, removing tracer diffusion causes important changes to each of these fields. While the surface signature of the western boundary current changes only slightly (i.e., it is a little weaker), the equatorial cold tongue and accompanying westward flow all but vanish (Fig. 17b). The SSOM run without tracer diffusion also produces a much shallower thermocline with a stronger temperature gradient (Fig. 17b), which is consistent with the sensitivity of thermocline depth in z-coordinate ocean models to vertical diffusivity (e.g., Bryan, 1987). Finally, the SSOM run without tracer mixing exhibits overturning of a fundamentally different nature (compare Fig. 19a and b). In the run with temperature diffusion there is vigorous overturning near the northern boundary that is approximately in a steady state by 700 years (Fig. 19a), but in the run without tracer mixing the northern most cell continues to weaken with time, and it has mostly disappeared by 700 years (Fig. 19b). Moreover, in the former case very cold water circulates upward into the equatorial thermocline (Fig. 19a), but in the latter case the overturning primarily amounts to shallow, wind forced cells (Fig. 19b). As noted by Boccaletti et al. (2005), the amplitude of heat transport is related to the perturbation in temperature following closed streamlines of meridional flow. In the run without tracer diffusion, individual streamlines span a much smaller temperature range (Fig. 19), and average northward heat transport from 10 to 40 N is reduced from 0.85 PW to 0.30 PW, that is, by almost a factor of 3 (Fig. 20). Because this model lacks important features of the Atlantic Ocean (e.g., the Antarctic Circumpolar Current), it is premature to assume that these results are directly applicable to heat transport in the Atlantic. However, they do illustrate one of the important potential uses for the SSOM – exploring how circulations and heat transport change in the no-tracer-diffusion limit.
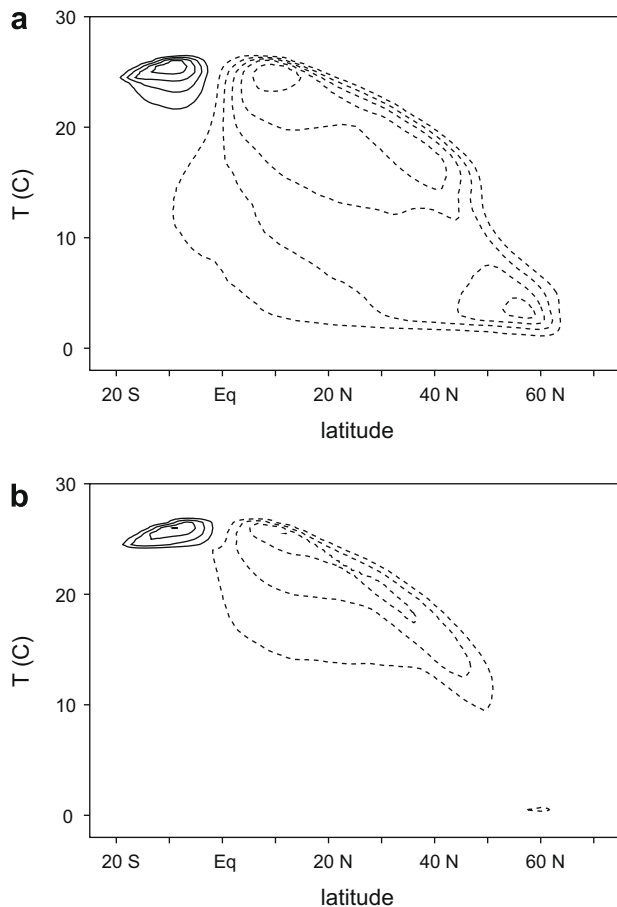
Fig. 19. Meridional overturning (3 Sv contours) for lower-resolution SSOM runs with (a) and without (b) tracer mixing.
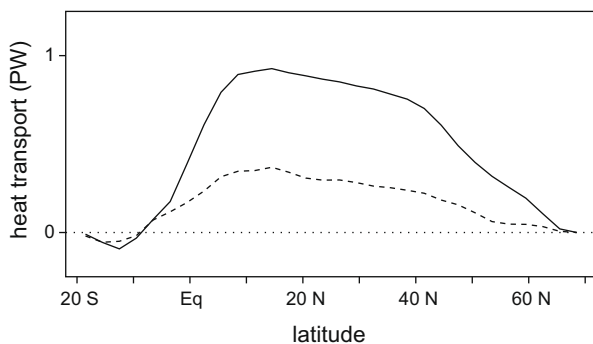

Fig. 20. Northward heat transport for the lower-resolution SSOM runs with (solid) and without (dashed) tracer mixing.

7. Summary and discussion

In this study we further develop the slippery sacks ocean model (SSOM), and we use it to simulate western boundary currents in homogeneous oceans and to model wind-forced gyres and meridional overturning in an idealized model the North Atlantic Ocean.

A new model feature that is introduced for this study is horizontal mixing. Sacks are allowed to exchange momentum with their nearest neighbors in the x- and y-directions. Tests reveal that the mixing scheme behaves similarly to traditional finite-difference diffusion in Eulerian models.

We test the model's ability to reproduce the Stommel and Munk solutions to the classical western boundary current problem. In linear regimes the model generates circulations that are consistent with theory, and in moderately non-linear regimes the model produces appropriate departures from linear solutions, including a boundary current that continues along the northern boundary for a time. We find that the key to producing reasonable results is to reduce potential energy barriers (PEBs) to sacks crossing over one another, which can be done in two ways: (1) by using vertically thin sacks; and (2) by reducing the amplitude of gravity.[10] We find that including horizontal viscosity also helps to reduce noise generated by PEBs.

Taking advantage of the new mixing scheme and lessons learned from simulations of homogeneous oceans, we construct an idealized model of the North Atlantic Ocean. We compare simulations conducted with the SSOM to similar simulations conducted with the Massachusetts Institute of Technology general circulation model (MITgcm). The SSOM and the MITgcm produce similar wind-forced gyres, thermocline structure, and meridional overturning. The SSOM is also used to explore how circulations change in the limit when tracer diffusion goes to zero.

Overall, this study represents several additional steps in the development of a full-fledged Lagrangian oceanic general circulation model that has certain capabilities that distinguish it from all other existing ocean models. Moreover, the simulations presented here provide a better understanding of the circumstances under which piles of slippery sacks behave like oceans, and will provide guidance for future simulations conducted with the SSOM.

Acknowledgments

References

Boccaletti, G., Ferrari, R., Adcroft, A., Ferreira, D., Marshall, J., 2005. The vertical structure of oceanic heat transport. Geophys. Res. Lett. 32, L10603. doi:10.1029/2005GL022474.
Bryan, K., 1963. A numerical investigation of a nonlinear model of a wind-driven ocean. J. Atmos. Sci. 20, 594–606.
Bryan, F., 1987. On the parameter sensitivity of primitive equation ocean general circulation models. J. Phys. Oceanogr. 17, 970–985.
Follows, M.J., Ito, T., Marotske, J., 2002. The wind-driven, subtropical gyres and the solubility pump of CO_2. Global Biogeochem. Cycles 16. doi:10.1029/2001GB0001786.
Griffies, S.M., Pacanowski, R.C., Hallberg, R.W., 2000. Spurious diapycnal mixing associated with advection in a z-coordinate ocean model. Mon. Wea. Rev. 128, 538–567.
Haertel, P.T., Randall, D.A., 2002. Could a pile of slippery sacks behave like an ocean? Mon. Wea. Rev. 130, 2975–2988.
Haertel, P.T., Randall, D.A., Jensen, T.G., 2004. Simulating upwelling in a large lake using slippery sacks. Mon. Wea. Rev. 132, 66–77.
Ierley, G.R., 1987. On the onset of inertial recirculation in barotropic general circulation models. J. Phys. Oceanogr. 17, 2366–2374.
Ito, T., Deutsch, C., 2006. Understanding the saturation state of argon in the thermocline: the role of air-sea gas exchange and diapycnal mixing. Global Biogeochem. Cycles 20, GB3019.
Jensen, T.G., 1996. Artificial retardation of barotropic waves in layered ocean models. Mon. Wea. Rev. 124, 1272–1283.

---

[10] The Stommel and Munk simulations are carried out with a homogeneous ocean, and steady solutions are only weakly sensitive to the value of gravity used. In more realistic circumstances gravity wave retardation (Jensen, 1996) can be applied to achieve the same effect.

Jensen, T.G., 2001. Application of the GWR method to the tropical oceans. Mon. Wea. Rev. 129, 470–484.

Jensen, T.G., 2003. Barotropic mode errors in an Indian Ocean model associated with the GWR method. Global Planet. Change 37, 3–20.

Park, Y., Bryan, K., 2000. Comparison of thermally driven circulations from a depth-coordinate model and an isopycnal-layer model. Part I: scaling-law sensitivity to vertical diffusivity. J. Phys. Oceanogr. 30, 590–605.

Pedlosky, J., 1987. Geophysical Fluid Dynamics. Springer-Verlag. 710 pp.

Pedlosky, J., 1996. Ocean Circulation Theory. Springer-Verlag. 453 pp.

Krauss, Wolfgang, 1973. Methods and Results of Theoretical Ocenography. I: Dynamics of the Homogeneous and the Quasi-homogeneous Ocean. Gebruder Borntrager. 302 pp.

Munk, W.H., 1950. On the wind-driven circulation. J. Meteorol. 7, 79–93.

Sheremet, V.A., Ierley, G.R., Kamenkovich, V.M., 1997. Eigen analysis of the two-dimensional wind-driven ocean circulation problem. J. Mar. Res. 55, 57–92.

Sheremet, V.A., 2002. A method of finding unstable steady solutions by forward time integration: relaxation to a running mean. Ocean Modell. 5, 77–89.

Stommel, H., 1948. The westward intensification of wind-driven ocean currents. Trans. Am. Geophys. Union 29, 202–206.

Sverdrup, H.U., 1947. Wind-driven currents in a baroclinic ocean with application to the equatorial currents of the eastern Pacific. Proc. Natl. Acad. Sci. USA 33, 318–326.

Veronis, G., 1966. Wind-driven ocean circulation – part 2. Numerical solutions of the non-linear problem. Deap Sea Res. 13, 31–55.